JOURNAL OF GEOPHYSICAL RESEARCH, VOL. 106, NO. C8, PAGES 16,903–16,915, AUGUST 15, 2001

Water depth and surface current retrievals from airborne optical measurements of surface gravity wave dispersion

J. P. Dugan, C. C. Piotrowski, and J. Z. Williams

Areté Associates, Arlington, Virginia, USA

Abstract. Visible images of nearshore ocean waves obtained from an aircraft have been utilized to estimate the surface currents and water depth below the waves. A digital framing camera was mounted in a motion-stabilized turret and used to obtain temporal sequences of high-quality optical images of shoaling ocean waves. Data on the position and attitude of the camera/turret were used to map the image data to a rectilinear coordinate system at the level of the surface, effectively separating the spatial and temporal modulations due to the waves. The resulting three-dimensional (3-D) space-time data sets were Fourier transformed to obtain frequency-wave number spectra of these modulations. These spectra contain information on the propagation characteristics of the waves, such as their wavelengths and frequencies, and their directions and speeds of propagation. The water depth and current vector have been estimated by choosing these parameters so that a "best" fit is obtained between the theoretical dispersion relation for linear gravity waves and these 3-D wave spectra. Image data sets were acquired during the Shoaling Waves Experiment (SHOWEX) along the quasi-linear coastline in the vicinity of the Army Corps of Engineers' Field Research Facility (FRF) near Duck on the North Carolina Outer Banks. Summary wave parameters and bathymetry and current retrievals are typically within 10% of contemporaneous in situ measurements, though outliers occur.

1. Introduction

Images of the ocean in the visible range of the electromagnetic spectrum have for many years provided qualitative and/or quantitative information on a number of parameters and physical processes associated with waves and wind. Since cameras and other optical imaging systems typically have excellent spatial resolution, data can be collected from moderate ranges that easily resolve the band of wavelengths associated with gravity waves. High-quality measurements have been made of the spatial spectrum of the longest surface gravity waves, or swell [e.g., *Barber*, 1949; *Stilwell*, 1969; *Stilwell and Pilon*, 1974], and the frequency-wave number spectrum of more moderate length gravity waves [*Lubard et al*., 1980; *Irani et al*., 1986] and small-scale gravity-capillary waves [*Jähne and Riemer*, 1990], all from stationary platforms near the water surface. Optical measurement systems have also been utilized in wave tanks with great success [e.g., *Keller and Gotwols*, 1983; *Jähne and Riemer*, 1990]. In addition, optical measurements of the wavelength and/or frequency (or, equivalently, the speed) of the resolved waves have been used to estimate the water depth.

This latter application was developed and used by the western allies during World War II, strongly motivated by the need to remotely survey the bathymetry off defended beaches [*Williams*, 1946; *Seiwell*, 1947]. The basic technique was to fly over the nearshore and take photographs of the waves as they approached the beach. The lengths and speeds of the longer waves decrease as they propagate into shallow water. If one knows the frequency of a dominant narrow-banded swell, which can be obtained from an image by measuring the wavelength in deep water, then the wavelengths measured from a single photograph can be used to estimate the water depth profile as the waves shoal. On the other hand, even without knowledge of the dominant frequency of the swell, one can estimate the depth from two images separated in time by measuring the local wave speed c and obtaining the depth from the surface gravity wave dispersion relation,

$$\omega = (g\kappa \tanh[\kappa h])^{1/2} + \mathbf{U} \cdot \boldsymbol{\kappa}, \tag{1}$$

where the frequency ω is $2\pi/T$, where T is the wave period; the scalar wave number magnitude $\kappa = 2\pi/\lambda$, where λ is the wavelength; $\boldsymbol{\kappa}$ is the wave number vector; g is the acceleration due to gravity; $\mathbf{U}$ is the water velocity vector (assumed constant and not a function of depth); h is the local water depth (also assumed locally constant); and

$$c = \omega/\kappa. \tag{2}$$

In this early application the currents were assumed to be nil. A significant source of error with these techniques was poor image registration due to limited knowledge of the actual position and attitude of the camera. Another problem was the assumption of narrow-banded swell. Often, the wave spectrum at sea is made up of a complex combination of wind waves and swell from multiple weather systems, making it difficult to identify a single dominant wavelength. These are not fundamental limitations and, in our view, the value of using optical images for this application has hardly begun to be explored using modern technology.

More recent work has been done using a variety of optical sensors to provide wave measurements and retrieve water depths. The phase speeds of shoaling waves have been estimated from imagery obtained by tower-mounted video cameras, and the water depth has been inferred using the dispersion relation [*Lippmann and Holman*, 1991; *Williams and Dugan*, 1997; *Stockdon and Holman*, 2000]. The dispersion

Paper number 2000JC000369.
0148-0227/01/2000JC000369$09.00

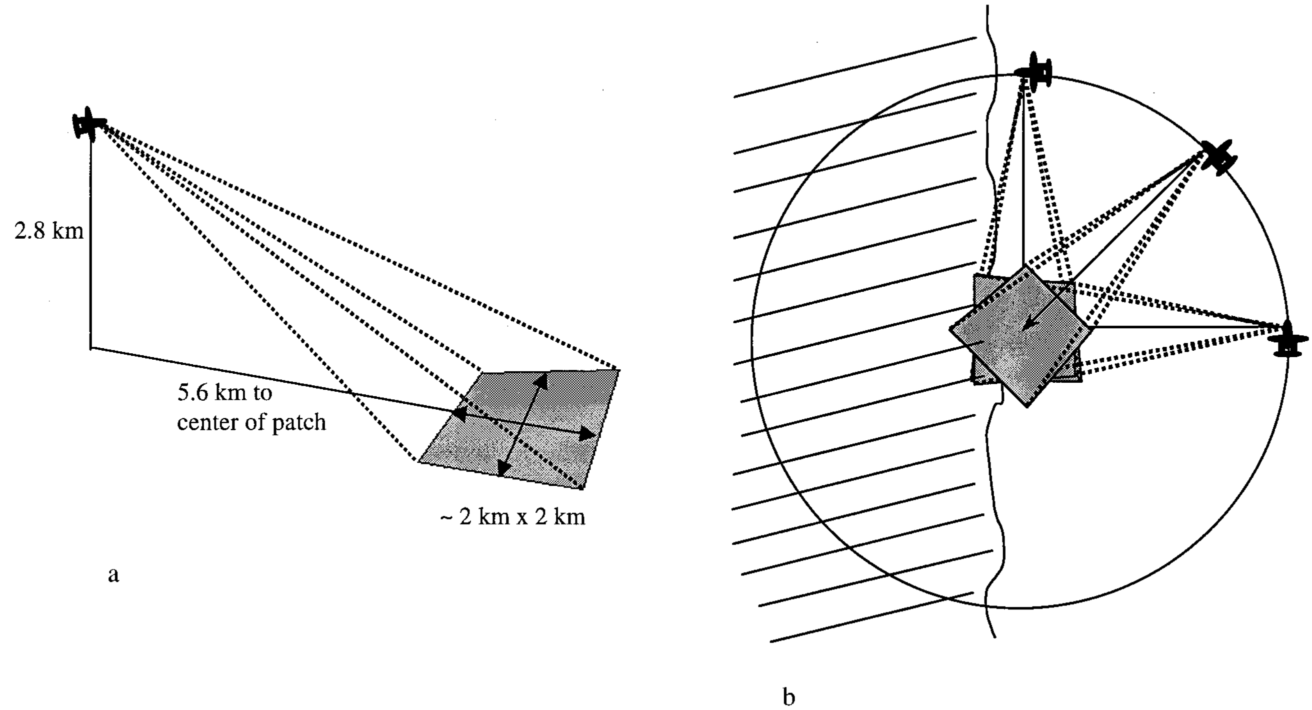

Figure 1. (a) Perspective view of the collection geometry. The aircraft altitude is 2.8 km, and the radius of its orbit is 5.6 km, resulting in a footprint on the ground of ~2 km × 2 km. (b) Overhead view along a shoreline. Cross hatch indicates land.

surface for deep water as well as shoaling waves was detected using an airborne optical system working in the infrared from ~85 km range [*Dugan et al.*, 1996], and these data were used to estimate the water depth [*Dugan*, 1997], though with errors as large as 30% of indicated depth. Others have attempted to use individual satellite images [*Leu et al.*, 1999; *Wu and Juang*, 1996] with what essentially is an application of the World War II technique, and again, the reported results appear to have limited accuracy.

In the field of radar remote sensing the propagation characteristics of nearshore waves have previously been utilized to estimate water currents, both with microwave radars that image the waves [*Young et al.*, 1985] and high-frequency radars that estimate the Doppler shift of a single or a small number of particular wavelengths [*Barrick*, 1980; *Teague*, 1986]. The technique using high-frequency radar has advanced to the point where commercial products are available for measuring surface currents. The Ocean Surface Current Radar (OSCR) and the Coastal Ocean Radar (CODAR) have been used for research and operationally. These high-frequency radar systems have proven to be successful for many researchers, although their rather poor spatial resolution limits their usefulness for nearshore variations of the currents. Since the work of *Young et al.*, [1985], there has been continuing effort to use microwave radars that are mounted near the coast to image waves, estimate the dispersion relation, and retrieve bathymetry and/or currents [e.g., *Lamont-Smith*, 1996; *McGregor et al.*, 1997, 1998; *Bell*, 1998; *Reichert et al.*, 1999].

Optics potentially could be used in the same manner as these microwave radars, and visible imagery has been underutilized for this purpose. Although shallow grazing angles are a problem for tower-mounted sensors, this can be avoided by mounting the sensor on an airborne platform, where more moderate grazing angles can be used while still maintaining a reasonable standoff range. (See Figure 1 for a diagram of our nominal collection geometry.) The methodology is to collect a series of geographically referenced images, compute the three-dimensional (3-D) frequency-wave number spectrum of the waves, estimate the location of the wave dispersion surface, and extract the bathymetry and currents from the location of this surface. There is some urgency in pursuing concepts for remotely estimating these particular parameters, as there is a need by the U.S. Naval Oceanographic Office for this type of information in regions that are observable from a distance but not immediately accessible to survey vessels. In this case, remote retrievals of the waves, water depth, and currents along defended coastlines would be useful for archiving and for assimilation into operational coastal ocean wave and circulation forecasting models. Reasonably accurate bathymetry is a fundamental input for these models. A primary technological issue to doing this operationally from an airborne platform is the registration of the imagery. In addition, although the general methodology for extracting bathymetry and current information from the imagery is now well known, the quality of data from inexpensive optical cameras and positioning systems and the accuracy and robustness of algorithms to do this with any reliability are uncertain.

We have developed a small, turret-based airborne optical system to evaluate the possibility of using today's inexpensive off-the-shelf technology for solving these problems. The image registration problem has been approached with an integrated Global Positioning System/Inertial Navigation System (GPS/INS) for accurately measuring the position and attitude of the camera/turret. The image quality problem has been approached with a digital framing camera which has excellent resolution and high dynamic range and linearity. Finally, the algorithm issue has been addressed to the level of providing interesting initial results, though not solved in any detail, nor are reliability or robustness issues addressed in this initial effort. The Airborne Remote Optical Spotlight System (AROSS) has been designed and constructed with this specific purpose in mind [*Dugan et al.*, 2001a], and initial imagery data sets were collected during the Shoaling Waves Experiment (SHOWEX), which was conducted near the U.S. Army Corps of Engineers Waterways Experiment Station (WES) Field Research Facility (FRF) located on the North Carolina Outer Banks in October–December 1999.

A separate approach using modern optical measurement techniques from aircraft platforms is active light detection and ranging (LIDAR) to directly measure the distance between the aircraft, the ocean surface, and the bottom in clear water [e.g., *Koppari and Karlsson*, 1994; *Smith and West*, 1999]. These systems have enjoyed some commercial success in recent years because of their superior accuracy and high resolution for detailed survey applications, although they suffer a necessity to fly directly over the target area. The potential advantages of the passive camera technique are the ability to fly at modest to large stand off distances from the target area, the ability to work where the water is not clear, and the ability to measure currents and waves simultaneously. On the other hand, of course, the likely disadvantages of the camera technique are lower accuracy and lower spatial resolution.

Section 2 describes our approach in more detail, with a short summary of the instrumentation, then section 3 provides the analysis results for two data sets collected at SHOWEX. In addition, a preliminary comparison with in situ data shows the results to be promising, and finally, section 4 provides our conclusions.

2. Approach

The general approach is to capture images of the radiance field as viewed from moderate grazing angles between the ocean surface and the line of sight to the viewing position. For angles between, say, 15° and 40° the radiance that is received at the camera is dominated by the background sky radiance that is reflected from the ocean surface [*Walker*, 1994]. This radiance field is modulated spatially and temporally by the slopes of the waves as they propagate. The actual measured spatial and temporal motions of the waves on the image plane of the camera are distorted from rectilinear spatial coordinates by the perspective view of the camera, and they are only correctly recovered by careful registration of the data to an Earth coordinate system. This perspective distortion is accounted for by measuring and applying the viewing parameters, both the 3-D position and attitude angles of the camera, as well as the optics of the camera and lens. This is accomplished by mapping the data to a rectilinear coordinate frame at the mean vertical level of the ocean surface (see J. Z. Williams et al., manuscript in preparation, 2001, for the particulars). This mapping transform is reasonably straightforward to apply, and the resulting mapped frames of data, to first order, have the correct space and time variations associated with the underlying wave motions. Comparisons have been made of the locations of known targets that were placed on the ground at FRF with those computed from the imagery, and the absolute accuracy of the unaided navigation system is ~20 m [*Dugan et al.*, 2000] from 6 km range. This offset error is not crucial in the overall scheme, but it does drift over a couple of minutes by rates of up to 20 cm/s. While this drift has only a small effect on the depth estimate, it would be directly confused with a surface current if it were not corrected, so it is removed by remapping the frames so that fixed features on the beach do not drift. So, at present, retrievals of surface currents are limited to locations that are close to shore.

The data values are recorded as digital counts (0–4095), and they are not calibrated. They are proportional to units of radiant energy that reach the focal plane of the camera. They are related to the line-of-sight wave slopes, more or less linearly, but the actual values are also a function of the Fresnel reflection coefficient at the surface, the mean and gradient in radiance of the background sky, emission at the surface, and absorption and reradiation of the intervening atmosphere [*Walker*, 1994]. The sky radiance gradient typically is not entirely linear, the Fresnel reflection coefficient is not constant but is a function of the slope, and the waves have nonlinear components, so the measured radiance has components that make a quantitative association with the linear ocean wave slopes rather unlikely [*Chapman and Irani*, 1981]. In addition, the pixels as mapped are not precisely located accurately in space because of a combination of the viewing perspective and the waves having finite amplitudes, a situation termed relief distortion, so the data contain additional nonlinear effects that must affect the mapped images to some degree. However, though these effects in combination make the retrieval of actual wave slopes rather unlikely, as noted previously, they are not so apparent in the data that the measurements are so significantly distorted that the variance is badly misplaced in the spectral domain. If the distortion were large, a significant amount of variance would appear at locations in the spectrum other than the linear dispersion surface, and this is not the case, as we will see later.

After mapping, the resulting 3-D cubes of radiance data properly encode the space-time wave information of immediate interest. Subsets of these data cubes are Fourier transformed in the three dimensions, after windowing to reduce spectral leakage, and the resulting power spectrum is plotted in 3-D frequency-wave number coordinates. The dispersion surface that theoretically governs the wave motions in the presence of finite water depth and current is the 2-D surface defined by (1). Our primary interest is parameter extraction or retrieval, in which the parameters $\mathbf{U}$ and h are estimated by fitting this theoretical dispersion surface to the spectrum that is calculated from the data cubes. This theoretical expression is cylindrically symmetric around the frequency axis in the absence of a current, but it is tilted into the current direction by an amount that is proportional to the current magnitude. This effect is readily apparent only for the higher-frequency waves. In addition, the diameter of this cylindrical surface at the lower frequencies is inversely dependent upon the local water depth. For deep water with no currents it takes on the simpler well-known form:

$$\omega = (g\kappa)^{1/2}. \tag{3}$$

In this methodology, the magnitude of the spectrum (i.e., the power on the dispersion surface) is proportional to the square of the amplitude of the waves but also is dependent upon other parameters, such as the sky gradient and viewing angles, so the power is not simply related to the actual wave amplitude spectrum. This does not affect the location of the dispersion surface, so it does not affect the retrieval problem except as it relates to the wave contrast, which we define as the peak

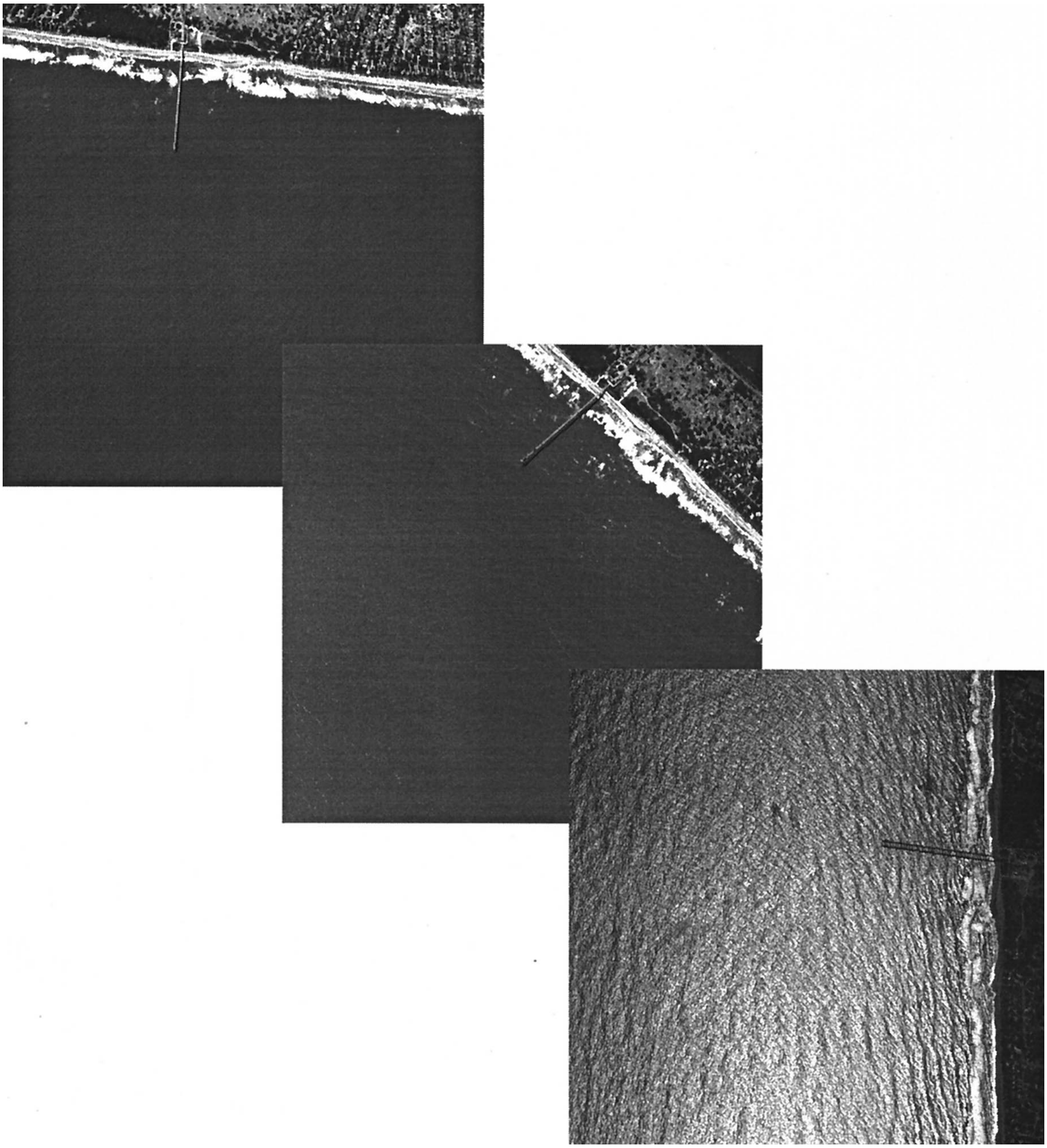

Figure 2. Raw Airborne Remote Optical Spotlight System (AROSS) data frames corresponding to the collection geometry illustrated in Figure 1b. The top image shows an onshore look, the middle image is ~45° to shoreline, and the bottom image shows an alongshore look.

energy on the dispersion surface relative to the nearby noise floor, a value that does ultimately affect the accuracy of the results. Thus the specific scattering mechanism, the form of the background sky gradient, and other physical causes of surface roughness modulations are not of overriding importance as long as these do not cause nonlinear effects that directly affect the location of the linear component of the wave spectrum. Effects of these forms have been mentioned in the past [*Walker*, 1994; *Chapman and Irani*, 1981; *Jähne*, 1993], but we assume here that these effects on the modulations of the received signal typically are nonlinearly related to the primary waves. Thus harmonics or "beats" are generated. These appear at distinct locations in the 3-D spectra that often are removed from the position of the linear dispersion surface of the pri-

Table 1. Environmental Conditions at Field Research Facility

Parameter	Oct. 19, 1999	Nov. 4, 1999
Time, UTC	1527	2045
Significant wave height, m	1.2	0.6
Swell frequency, Hz	0.103	0.113
Swell period, s	9.71	8.87
Swell direction, °T	78	96
Swell spectral contrast, dB	35	30
Tide height, m	0.20	0.28
Wind speed, m/s	4.5	3.7
Wind direction, °T	43.5	204
Sun azimuth, deg east of south	26.5	−58.9
Sun elevation, deg	40	14

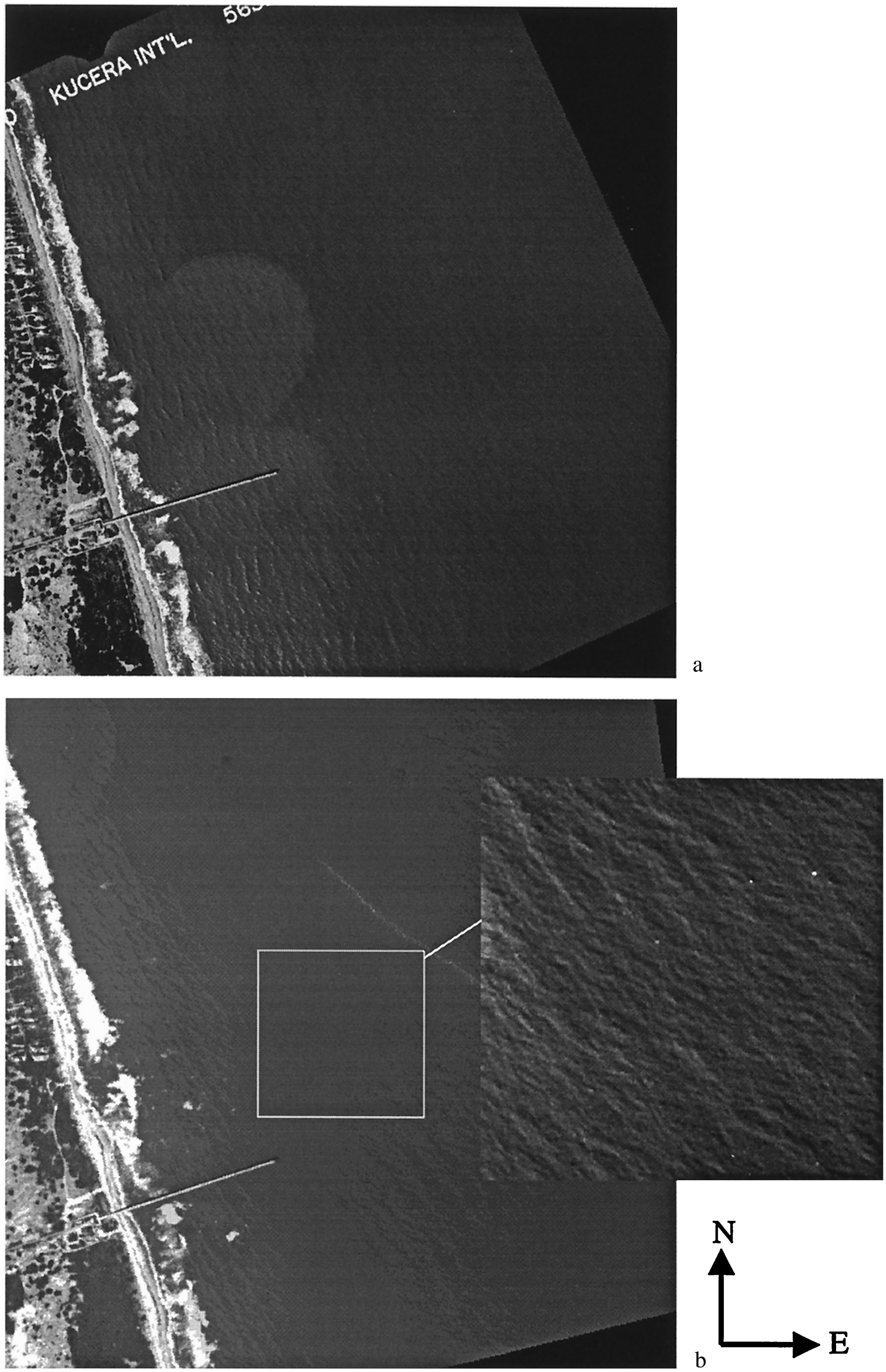

Figure 3. (a) Aerial survey photo. (b) Mapped AROSS image and a closeup of the processed subset.

mary waves and do not affect its location in ω-κ space or significantly reduce the wave contrast.

Ideally, the fit of the dispersion surface would be performed in three dimensions simultaneously. In practice, low-frequency, low–wave number noise often contaminates the spectra (for example, surfactant streaks), resulting in difficulty in obtaining good depth estimates since it is primarily the longest waves which are significantly affected by the bottom. Therefore, for this paper, the fit of the dispersion relation is accomplished for 2-D ω-κ slices which can be chosen to avoid regions of high

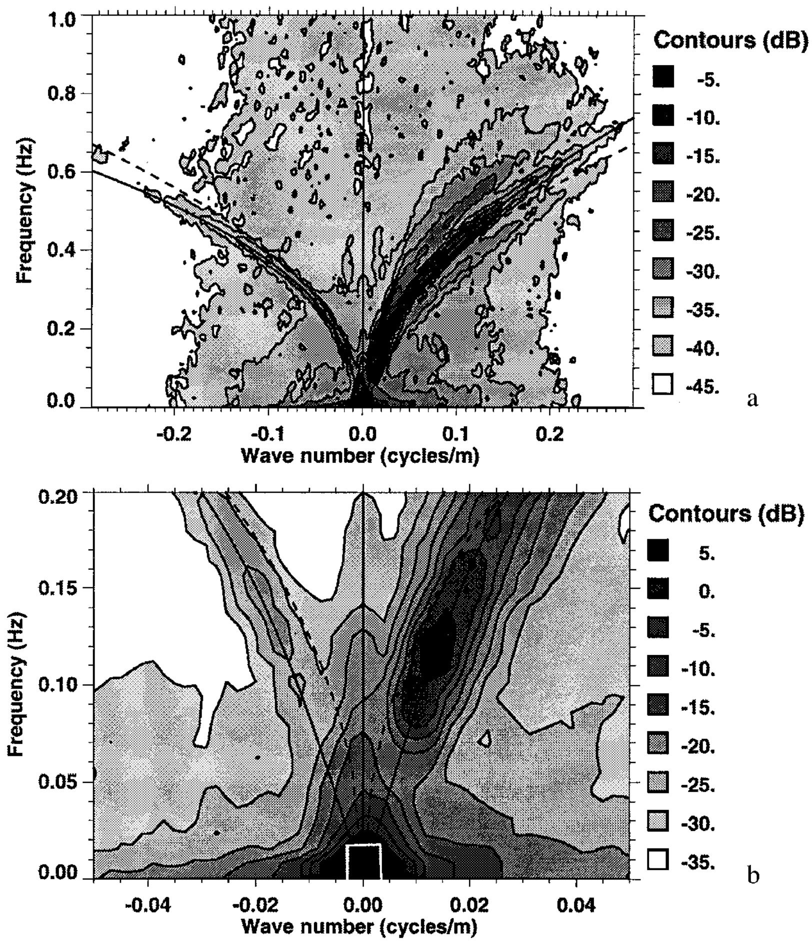

Figure 4. (a) Frequency-wave number (f-k) slice in the direction of the swell, with both the deep water dispersion relation (dashed curve) and the empirical fit (solid) to the spectrum with depth $h = 8.2$ m and current $U = 0.14$ m/s in the direction of the swell. (b) Closeup of the low-frequency and wave number portion of the spectrum, showing the fit (solid line) versus the deep water dispersion curve (dashed line).

noise. For each κ value of a slice we find the ω value with the maximum spectral energy and then perform a nonlinear least squares fit of the form of the two-parameter (h and **U**) function given by the dispersion relation (equation (1)). We first perform the fit for the ω-κ slice in the direction of peak wave energy at low frequency-wave number (the direction of swell propagation) in order to obtain the best estimate of the depth since those are the waves that are most affected by the bottom. Then, to obtain the component of the current in specific directions, which may not have enough energy at low frequency and wave number to produce a good depth estimate, the depth is held fixed, and only the current is allowed to vary when obtaining the fit in those ω-κ slices.

This general Fourier method enjoys the important benefit of the multiple degrees of freedom that many wavelengths (or frequencies, equivalently) in the wave spectrum contribute to the dispersion surface. Thus multiple frequency-wavelength pairs contribute to the parameter estimation, providing considerable noise reduction and robustness to the procedure. Also, since all directional information of the waves is retained, there is no confusion among a number of different wave trains, as often occurs when the waves are assumed to consist of a single dominant component. Thus, no matter their propagation direction, all waves contribute positively to the confidence in the fit. Finally, the amount of data and the smoothing that is applied are important as well. For example, the width of the spectral ridge is inversely proportional to the size of the data cube in physical space and time. Within limits, the longer the temporal dwell and the larger the spatial domain, the narrower the ridge of energy along the dispersion surface. This can be quantified by the formula

$$\delta h/h = g(\kappa h)\ \delta\kappa/\kappa + f(\kappa h)\ \delta\omega/\omega, \qquad (4)$$

where the functions f and g are given by *Dalrymple et al.* [1998] and these functions have numerical value of order 2 when κh is small. This expression is obtained using variational methods after solving (1) for the depth (assuming no current). The term δh is the depth variation, $\delta\kappa$ is the wave number variation, which is inversely proportional to the size of the spatial domain, and $\delta\omega$ is the frequency variation, which is inversely proportional to the temporal length of the data set, or dwell. Thus, relating resolution with variations, the depth uncertainty is proportional to the uncertainty in both wave number and frequency. Improving both the frequency and wave number resolution improves the depth resolution as long as both contribute, but very large improvements in one or the other are not particularly beneficial. This is elementary multidimensional spectral analysis, and as is well known, the relation must be taken with some reserve since there is an inherent assumption that the waves and all parameters are homogeneous in space and stationary in time, i.e., the current and depth are constant over the 3-D space-time cube. It also assumes that the response function for the waves is constant over the dwell, and this noticeably is not true for large changes in azimuth that occur over long dwell. The assumption of no current in (4) is not important in this discussion, as it simply tilts the dispersion surface away from symmetry around the frequency axis and this has no great impact on the width of the ridge of energy near the dispersion surface in the 3-D spectrum.

Since both currents and depth can vary over the nearshore, one has to be judicious in choosing the size of the subpatch that is being Fourier analyzed based on the expected variations in these parameters. The larger the area being Fourier analyzed, the better the spectral resolution, and therefore the better precision on the location of the dispersion surface. On the other hand, where the bathymetry and current vary significantly on small scales, for instance, near an offshore bar, the homogeneity requirement is violated. In addition to increasing the width of the dispersion surface, inhomogeneity in depth introduces a shallow bias owing to the nonlinear dependence of wave speed on depth in the dispersion relation. Other than (4), we have no guidance on balancing these conflicting requirements.

The sensor system that is utilized for this study is AROSS (see *Dugan et al.* [2001a] for a detailed description). In summary, it is comprised of a digital framing camera that is mounted in an inertially stabilized turret under the nose cone of a small aircraft. The turret is commanded by a computer controller to point from its present GPS position to the GPS position of a predetermined target at the level of the local mean water surface. The camera has a panchromatic (single gray scale) digital charge-coupled device (CCD) array having 1024 by 1024 elements and a 2:1 anamorphic lens. The sensitive elements of the focal plane array spatially fill it, so there is minimal spatial aliasing, but our typical exposure time is only ~10 ms, which leaves a long temporal gap between frames and thereby allows temporal aliasing of higher-frequency modulations. A sampling rate of 2 Hz is sufficient to avoid this for gravity wavelengths of 2 m and longer. The anamorphic lens approximately accounts for the projection of the field of view (FOV) onto a level geodetic surface from our nominal grazing angle of ~30° relative to the ocean surface, but the mapping procedure uses the precise attitude and camera optics to provide precisely located data. At our typical flight altitude and distance to the target the spatial resolution on the water is ~2 m, and the mapped FOV (patch) has a keystone shape because of the viewing geometry and is ~2 km × 2 km in size (see Figure 1). The aircraft flies around or past the target position, and the camera can collect continuous data on the same patch of ocean for up to many minutes of dwell.

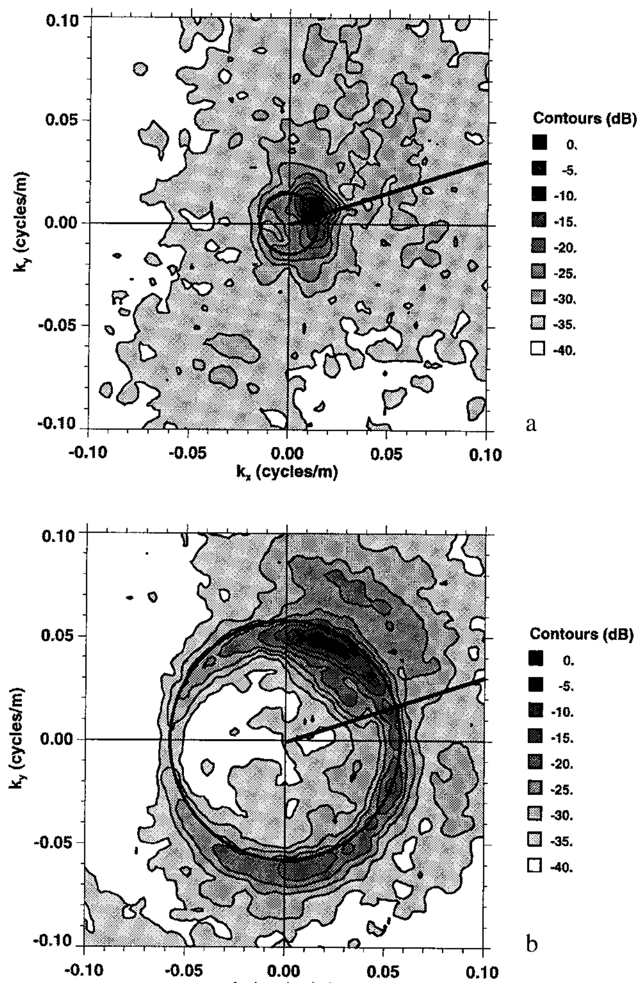

Figure 5. The k_x-k_y slice through the 3-D spectrum at the swell frequency of (a) 0.12 Hz and (b) at 0.3 Hz, near the dominant wind wave frequency. In these plots, k_x is east-west, and k_y is north-south. The dark solid line indicates the direction normal to the shoreline.

3. Data Collection, Analysis Procedures, and Results

SHOWEX was conducted in October–December 1999 in the coastal region near the U.S. Army Corps of Engineers' FRF on the Outer Banks at Duck, North Carolina. The primary emphasis of this experiment was the energy budget for the surface wave spectrum as the waves propagate across the wide, shallow shelf near Duck, but our imagery was largely focused on the nearshore at FRF. The water depth at this location varied from the beach to ~15 m, with a bottom slope of <1%. The depths were measured by coordinated surveys before and after our experiment by a combination of the FRF Coastal Research Amphibious Buggy (CRAB) and the FRF Lighter Amphibious Resupply Cargo (LARC). The CRAB crawls on the bottom and uses a kinematic GPS (KGPS) receiver for measuring the geodetic height of the bottom (see *Birkemeier and Mason* [1984] for an early description), and the LARC, a wheeled amphibious vehicle, uses a combination of a KGPS receiver and a fathometer for measuring these heights/depths [*Dugan et al.*, 1999, 2001b]. The retrieved depths were adjusted to account for the local tide level at the times of the remote observations, so that a direct comparison can be made between the retrieved depths and the survey depths. In situ water current profiles were measured during one of the observations reported in this paper. In addition, FRF measured the frequency–directional wave spectrum using an array of bottom pressure sensors near 8 m water depth and also measured the wind vector using an anemometer near the seaward end of their long pier. The measured wave spectra are valid only for frequencies lower than ~0.3 Hz owing to the exponential loss of pressure

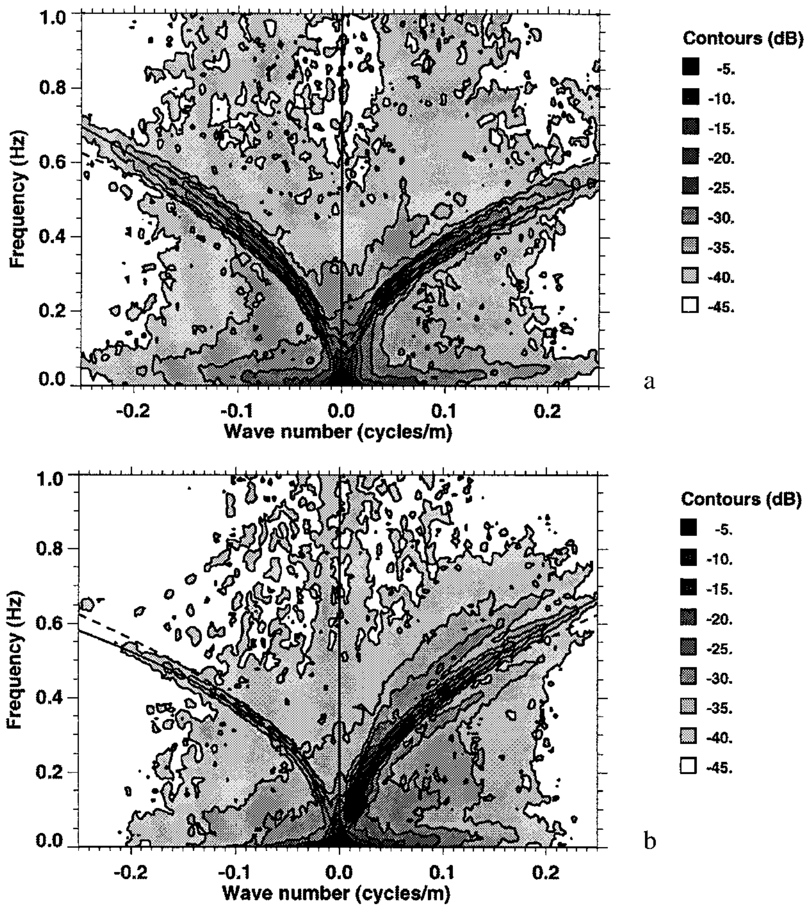

Figure 6. Estimation of (a) alongshore and (b) cross-shore current components. Dashed lines indicate the deep water/no current dispersion relation, and solid lines indicate the fit obtained for a current magnitude of 0.28 m/s alongshore toward the southeast (Figure 6a) and 0.17 m/s cross shore toward shore (Figure 6b).

modulations over the 8 m depth, but they are accurate for the longer and lower-frequency waves.

Two data sets are utilized in this paper, one collected at 1527 UTC on October 19, 1999, and the other collected at 2045 UTC on November 4, 1999. In both cases, the target point was the center of the FRF 8 m pressure array (36°11.23′N, 75°44.57′W). The aircraft circled the array for ~8 min, from an altitude of ~2.8 km and a radial distance from the aircraft to the target point of ~5.6 km, acquiring 1000 frames of data. Figure 1 illustrates the collection geometry from both a perspective view (Figure 1a) and an overhead view showing three positions along the aircraft's orbit (Figure 1b). The three raw AROSS images from the October 19 data set corresponding to these three aircraft positions are provided in Figure 2. Note the

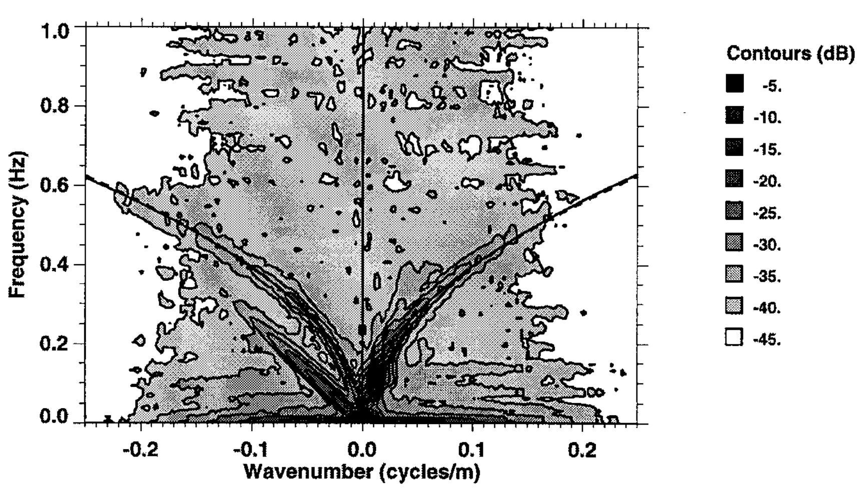

Figure 7. Frequency–wave number (f-k) slice in the direction of the swell for November 4, 1999.

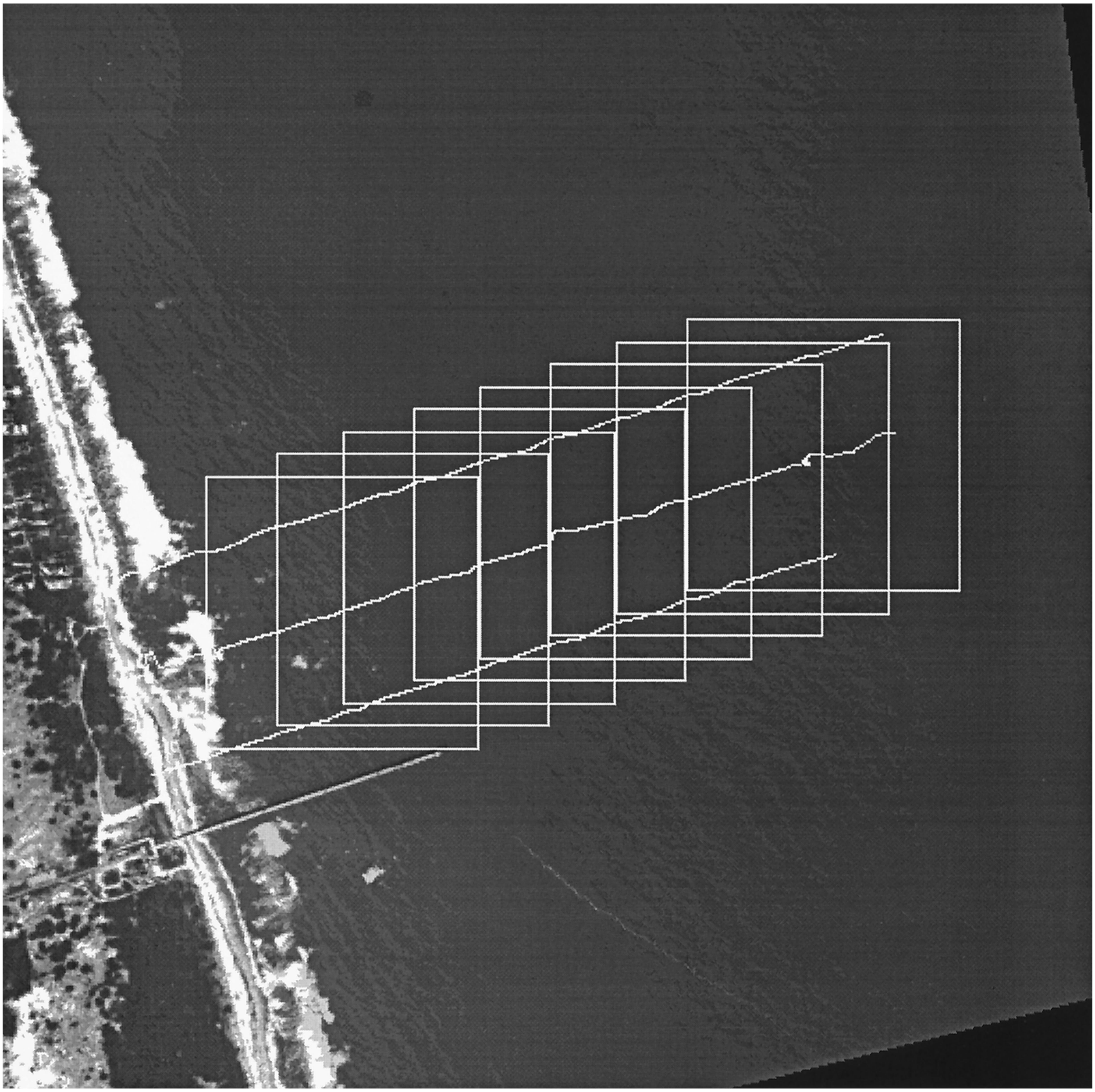

Figure 8. Processing subpatches and ground truth bathymetry survey lines.

linearity of the coastline, which implies that the bathymetry contours are also parallel to the beach, though likely with some variability in the vicinity of the nearshore bar and trough, and the FRF pier, which points toward 072°T. Also note the change in wave contrast in the third image, as the look direction turns toward the Sun and the glitter pattern. The data in the analyses reported here were collected away from the Sun. Environmental conditions at FRF for each data set are listed in Table 1.

A 2 min segment of each data set was selected for processing and mapped to a north-east coordinate system at the vertical level of the local mean ocean surface. Figure 3b shows a sample of a mapped data frame from October 19 along with an image of the area that was obtained a few days later by an aerial survey camera (Figure 3a). In most of the images in both Figures 2 and 3, the waves are not immediately obvious because of the large range of luminance levels that are required to keep the bright land on scale in the image. Thus Figure 3b also illustrates a portion of the scene outside the surf line in which the scale is expanded and the histogram of the wave-related data has been stretched to cover the same radiance scale as the rest of the image. Waves having a broad range of lengths are readily apparent.

Figures 4–6 display slices through the 3-D ω-κ power spectrum obtained using the October 19 data set. The 256 $\times$ 256 pixel patch ($\sim$500 $\times$ 500 m) centered on the FRF 8 m directional wave array and shown in Figure 3b was chosen for processing. The data were spatially detrended and frame-by-frame mean normalized, and a 10% cosine taper was applied. A 3-D fast Fourier transform (FFT) was performed, and the power spectrum was calculated and smoothed using a 3 $\times$ 3 $\times$ 3 band boxcar. The 95% confidence interval given this amount of smoothing (54 degrees of freedom) is [0.66, 1.41] times the indicated value of the spectrum. Figure 4a shows a 2-D f-k slice through the resulting power spectrum in the primary

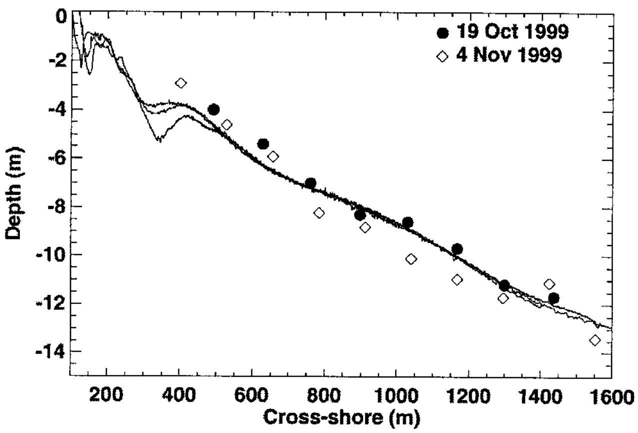

Figure 9. Comparison of water depth estimated from AROSS data (circles and diamonds) and ground truth bathymetry survey data (lines). The AROSS depth retrievals have been adjusted to account for the measured tide at the time of data collection.

direction in which the swell is propagating, with the wave number axis nearly normal to the shore, where the frequency $f = \omega/2\pi$ (in Hz) is shown versus the wave number $k = \kappa/2\pi$ (in cycles/m). In this plot, waves approaching the shore appear on the positive wave number (right) side of the spectrum, while waves traveling in the opposite direction appear on the negative wave number side. The waves occupy a wide range of frequencies from the swell near 0.1 Hz (wavelength near 100 m) almost all the way out to a frequency of ~0.5 Hz (wavelength near the Nyquist of 4 m). Note the narrowness of the ridge of energy (the dispersion surface) that lies along the smooth line which represents the fit to this dispersion surface with depth $h = 8.2$ m and current (in the direction of the slice) $U = 0.14$ m/s. The theoretical dispersion surface for zero current and infinite water depth is shown as the dashed line. There also are interesting sidebands near the primary waves that are ~10–15 dB below the level of the energy on the ridge. We believe the source of this sideband energy is relief distortion of the small but finite amplitude of the waves since it is typically associated with collections having higher waves and only in looks along the primary propagation direction. However, this does not rule out a hydrodynamic source, so it should be taken only as an initial hypothesis to be evaluated in depth in future work.

Figure 4b is the same spectral slice, but it expands the plot for the lower-frequency, longer-wavelength portion of the spectrum. The small box at the origin indicates the size of the smoothing window. Again, the dashed line is the dispersion relation for infinite depth and zero current, while the solid line is the fit to the spectrum using a depth of 8.2 m and passes directly through the center of the observed ridge of wave energy. For comparison, the average water depth measured by the FRF LARC over this 500 m region near the 8 m array was precisely 8.0 m, so the error of the retrieval for this case is <3%. Note also that there is much lower amplitude but clearly noticeable wave energy that is propagating in the opposite direction, presumably having been reflected by processes near the beach and/or in the surf. The reflected wave energy is also apparent in Figure 5, which displays constant frequency slices through the 3-D spectrum. In these plots the k_x and k_y axes are aligned with east and north, respectively, and wave energy appears at the direction the waves are coming from. Figure 5a is the slice at a constant frequency of 0.12 Hz, near the dominant swell frequency. The solid circular line is the intersection of the dispersion surface (assuming 8 m water depth and no current) and this spectral surface. Figure 5a clearly shows the direction of propagation of the incoming swell and the broad distribution of reflected waves at this frequency. The proportion of energy in the reflected waves relative to the incoming waves can be obtained by separately integrating the left and right sides of this spectral slice and taking the ratio of the two. In this particular case, the reflected wave energy is ~8% of the onshore energy. This is consistent with previous in situ measurements at this site using an array of bottom-mounted pressure sensors [*Elgar et al.*, 1994]. We believe that this is the first estimate of reflected wave energy obtained from optical imagery, and this was made possible by the high fidelity of the measurement system.

Figure 5b is a slice at a constant frequency of 0.3 Hz, which is near the dominant wind wave frequency. Again, the solid circular line is the intersection of the theoretical dispersion surface assuming no current and this spectral surface. This slice clearly shows that the dominant portion of these waves is traveling more parallel to the shoreline than is the swell and also has a broader directional distribution. In addition, the location of the energy is distorted from circular symmetry about the frequency axis (i.e., the circle center has been moved from [0,0]), presumably by a current that is oriented in the alongshore direction. The difference between the circular intersection of the theoretical dispersion surface for zero current and the virtual center of the observed circle representing the wave dispersion surface is directly related to the water velocity vector. Figure 6 shows the frequency-wave number slices in the alongshore direction (Figure 6a), with waves traveling alongshore from −18°T appearing on the left-hand side of the plot and waves traveling alongshore in the opposite direction (from 162°T) appearing on the right-hand side, and the cross-shore direction (Figure 6b), with waves heading on shore appearing on the right-hand side of the plot and waves heading off shore appearing on the left-hand side. It is immediately apparent that the cross-shore component is smaller than the alongshore component. The precise numbers that were retrieved by the fitting procedure were 0.17 m/s cross shore toward shore and 0.28 m/s alongshore toward the southeast.

For comparison, Figure 7 shows the *f-k* slice in the direction of swell propagation from the November 4 data set. The significant wave height was much lower for this data set (0.6 versus 1.2 m on October 19). It should be noted that the swell peak is ~5 dB lower than that of the October 19 data set and that the ridge of energy on the dispersion surface does not extend nearly as far into the high-frequency region of the spectrum. Also note the linear feature below the dispersion

Table 2. Summary Statistics of the Comparison Between Airborne Remote Optical Spotlight System (AROSS) Depth Estimates and the Ground Truth Bathymetry Survey, Calculated Using the Mean of the Survey Values Within Each Subpatch

Bathymetry	Oct. 19, 1999	Nov. 4, 1999
Bias, m	0.12	−0.45
RMS error, m	0.48	1.1
Mean relative error, %	5	13

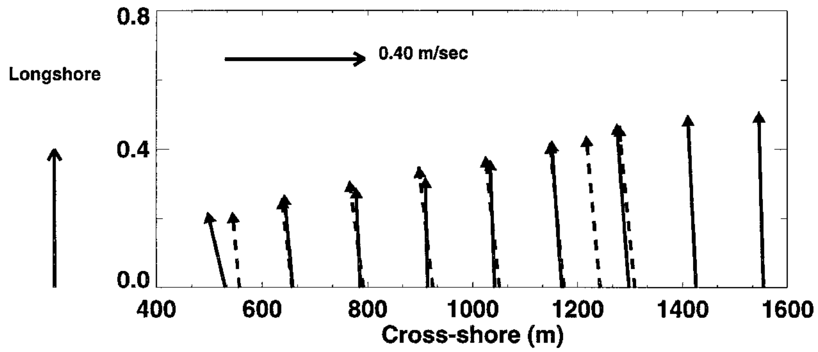

Figure 10. Retrieved AROSS current vectors (solid vectors) from November 4, 1999, and acoustic Doppler current profiler current vector measurements at 1.5 m depth (dashed vectors).

surface on the left side of the spectrum, which is due to the presence of our jet ski–based in situ current measurement system in the imagery, traveling directly offshore at a constant speed of 2.5 m/s.

In order to obtain depth profiles for comparison with the FRF bathymetry survey, overlapping subpatches were chosen as illustrated in Figure 8. The locations of the subpatches that were Fourier analyzed are indicated by the white squares, and the three approximately straight lines represent the locations of LARC bathymetry survey lines. Figure 9 shows a cross-shore plot of the depth profiles from the three survey lines and also the retrieved depths for each of the subpatches for the two data sets. The cross-shore distance is given in the FRF coordinate system, which is aligned with the orientation of the pier and mean shoreline. Summary statistics are given in Table 2. For the October 19 data set the differences are rather small for the entire extent of the ground truth survey. The November 4 data set gives similar results, although the errors are somewhat larger. This can be attributed to the lower wave energy and contrast observed during that data collection, as noted earlier, and it should be emphasized that environmental conditions clearly can affect the quality of bathymetry estimates that can be obtained. Although biases are observed, they are small relative to the RMS errors, suggesting that the shallow bias introduced by nonconstant depth is negligible in this region, as expected for such a shallow bottom slope.

Simultaneous in situ current measurements were collected on November 4 using a downward looking Acoustic Doppler Current Profiler (ADCP) that was mounted on the rear of a jet ski [*Dugan et al.*, 2001b]. The jet ski traversed the collection area in the cross-shore direction, along a line ~300 m north of the pier, at a speed of 2.5 m/s. The current measurements were collected in 0.5 m depth bins, with the shallowest bin ~1.5 m below the surface. Although the current varied systematically with distance from shore, it remained fairly constant at any given location for the duration of the ADCP collection, so 30 min averages were calculated to reduce wave-induced noise. In Figure 10 the AROSS velocity vector (solid vector) for each of the subpatches is plotted as a function of the offshore distance of the patch center, along with the ADCP current velocity measurement at 1.5 m depth averaged over each subpatch centered on the AROSS collection time (dashed vectors). The agreement is excellent, with mean differences of 1.3 cm/s in magnitude (4%) and 4° in direction (Table 3).

Finally, Table 4 compares the primary directions, periods, and frequencies of the peak values of the spectra for the two data sets with the values measured by the FRF directional wave array. Although the agreement is quite good on November 4 (within 5% in frequency and 5° in direction), we obtained about a 10% difference in frequency and 22° in direction with the October 19 data. It should be noted that the FRF values are obtained using data collected over a 136 min time period, compared to the 2 minute segments of AROSS data used here. In addition, preliminary investigation has shown that the details of the AROSS spectra are dependent on the viewing angle relative to both the Sun and the direction of wave propagation, and further analysis will be required in order to quantify and understand this dependence.

4. Conclusions

In conclusion, modern, rather inexpensive components have been successfully integrated to provide high-quality space-time data on the propagation of shoaling waves. This initial analysis of AROSS data has produced highly resolved ω-κ spectra, which could only result from the combination of the high-quality camera, accurate mapping, fine sampling, long dwell, and large subpatches that were analyzed. All of these elements are necessary to obtain high resolution and a narrow ridge of

Table 3. Summary Statistics of the Comparison Between AROSS Current Estimates From November 4, 1999, and Simultaneous Acoustic Doppler Current Profiler Current Measurements

Currents	Nov. 4, 1999
Mean error in magnitude, cm/s	1.3 (4%)
RMS error in magnitude, cm/s	1.6
Mean error in direction, deg	3.8
RMS error in direction, deg	4.4

Table 4. Comparison of FRF Directional Wave Measurements With AROSS Retrievals

	Oct. 19, 1999		Nov. 4, 1999	
Parameter	FRF	AROSS	FRF	AROSS
Swell frequency, Hz	0.103	0.117	0.113	0.109
Swell period, s	9.71	8.55	8.87	9.17
Swell direction, °T	78	56	96	91

energy that represents the dispersion surface. The narrowness of this ridge and the resulting high power level relative to the noise (i.e., high wave "contrast") enable a very accurate and precise estimate to be made of the location of the dispersion surface. The theoretical dispersion surface was fit to the observed surface, using a very simple algorithm, and quite accurate depth and current retrievals obtained. The depth retrievals compare very well with the bathymetry survey between 4 and 12 m in depth, having RMS errors of 0.5–1 m, or ~5–13%. This is quite adequate for quick survey applications of the nature described in section 1. Of course, lower wave energy and shorter wavelengths result in less accurate depth retrievals. The retrieved surface currents also compare very well with the in situ ADCP measurements, with RMS errors of <5% in magnitude and just a few degrees in direction. We expect that even higher accuracy could be achieved with a more sophisticated algorithm which takes advantage of the full three-dimensional extent of the dispersion surface. We obtained somewhat mixed results in comparing the retrieved directions, periods, and frequencies of the primary wave systems with the in situ values from the FRF 8 m pressure array, and further analysis is needed to determine the primary cause of the differences between the two.

Finally, we should repeat our earlier caution that these products can be achieved only when there are gravity waves present, as the waves provide the information required to retrieve the bathymetry and currents. One should not expect to be able to use the method in sheltered areas where there are no long gravity waves of significance. On the other hand, in those locations where there usually are waves, such as along exposed beaches and inlets, the results do not depend upon water clarity, so the method represents an alternative to airborne LIDAR depth measurements.

Acknowledgments. This work was funded by the Office of Naval Research. The U.S. Army Corps of Engineers Field Research Facility, Duck, North Carolina, provided excellent facilities, support, and in situ data.

References

Barber, N. F., A diffraction analysis of a photograph of the sea, *Nature*, *164*, 485, 1949.

Barrick, D. E., Accuracy of parameter extraction from sample-averaged sea-echo Doppler spectra, *IEEE Trans. Antennas Propag.*, *AP-28*, 1–10, 1980.

Bell, P. S., Bathymetry derived from an analysis of X-band marine radar images of waves, in *Proceedings of Oceanology International '98*, vol. 3, pp. 535–543, Spearhead Exhibitions, Ltd., London, 1998.

Birkemeier, W. A., and C. Mason, The CRAB: A unique nearshore surveying device, *J. Surv. Eng.*, *110*, 1–7, 1984.

Chapman, R. D., and G. B. Irani, Errors in estimating slope spectra from wave images, *Appl. Opt.*, *20*, 3645–3652, 1981.

Dalrymple, R. A., A. B. Kennedy, J. T. Kirby, and Q. Chen, Determining depth from remotely-sensed images, in *Coastal Engineering 1998: Proceedings of the 26th International Conference*, vol. 2, pp. 2395–2408, Am. Soc. of Civ. Eng., New York, 1998.

Dugan, J. P., Bathymetry measurements from long range airborne imaging systems, paper presented at 4th International Conference on Remote Sensing for Marine and Coastal Environments, Environ. Res. Inst. of Mich., Orlando, Fla., March 17–19, 1997.

Dugan, J. P., H. H. Suzukawa, C. P. Forsyth, and M. S. Farber, Ocean wave dispersion surface measured with airborne IR imaging system, *IEEE Trans. Geosci. Remote Sens.*, *34*(5), 1282–1284, 1996.

Dugan, J. P., K. C. Vierra, W. D. Morris, G. J. Farruggia, D. C. Campion, and H. C. Miller, Unique vehicles used for bathymetry surveys in exposed coastal regions, paper presented at Hydro'99, Hydrogr. Soc. of Am., Mobile, Ala., May 1999.

Dugan, J. P., A. E. Evans, and U. V. Bhapkar, Airborne image navigation for ocean wave motion analysis, paper presented at 2000 National Meeting, Inst. of Navig., Anaheim, Calif., Jan. 26–28, 2000.

Dugan, J. P., G. J. Fetzer, J. Bowden, G. J. Farruggia, J. Z. Williams, C. C. Piotrowski, K. Vierra, and D. Campion, Airborne optical spotlight system for remote sensing of ocean waves, *J. Atmos. Oceanic Technol.*, *18*(7), 1267–1276, 2001a.

Dugan, J. P., W. D. Morris, K. Vierra, C. C. Piotrowski, G. Farruggia, and D. Campion, Jet-ski based bathymetry and current survey system for nearshore use, *J. Coastal Res.*, *17*(3), 302–327, 2001b.

Elgar, S., T. H. C. Herbers, and R. T. Guza, Reflection of ocean surface gravity waves from a natural beach, *J. Phys. Oceanogr.*, *97*, 1503–1511, 1994.

Irani, G. B., B. L. Gotwols, and A. W. Bjerkaas, The 1978 Ocean Wave Dynamics Experiment: Optical and in situ measurement of the phase velocity of wind waves, in *Wave Dynamics and Radio Probing of the Ocean Surface*, edited by O. M. Phillips and K. Hasselmann, pp. 165–179, Plenum, New York, 1986.

Jähne, B., *Spatio-Temporal Image Processing: Theory and Scientific Applications*, 116 pp., Springer-Verlag, New York, 1993.

Jähne, B., and K. S. Riemer, Two-dimensional wavenumber spectra of small scale water surface waves, *J. Geophys. Res.*, *95*, 11,531–11,546, 1990.

Keller, W. C., and B. L. Gotwols, Two-dimensional optical measurement of wave slope, *Appl. Opt.*, *22*, 3476–3478, 1983.

Koppari, K., and U. Karlsson, Airborne laser depth sounding in Sweden, *Int. Hydro Rev. Monaco*, *81*(2), 69–90, 1994.

Lamont-Smith, T., The estimation of ocean current from ω-κ analysis of radar data, in *IGARSS '96: 1996 International Geoscience and Remote Sensing Symposium*, vol. 3, pp. 1742–1744, IEEE Press, Piscataway, N.J., 1996.

Leu, L.-G., Y.-Y. Kuo, and C.-T. Liu, Coastal bathymetry from the wave spectrum of SPOT images, *Coastal Eng. J.*, *41*(1), 21–41, 1999.

Lippmann, T. C., and R. A. Holman, Phase speed and angle of breaking waves measured with video techniques, *Coastal Sediments '91*, edited by N. Kraus, pp. 542–556, Am. Soc. of Civ. Eng., New York, 1991.

Lubard, S. C., J. E. Krimmel, L. R. Thebaud, D. D. Evans, and O. H. Shemdin, Optical image and laser slope meter intercomparison of high-frequency waves, *J. Geophys. Res.*, *85*, 4996–5002, 1980.

McGregor, J. A., E. M. Poulter, and M. J. Smith, Ocean surface currents obtained from microwave sea-echo Doppler spectra, *J. Geophys. Res.*, *102*, 25,227–25,236, 1997.

McGregor, J. A., E. M. Poulter, and M. J. Smith, S band Doppler radar measurements of bathymetry, wave energy fluxes, and dissipation across an offshore bar, *J. Geophys. Res.*, *103*, 18,779–18,789, 1998.

Reichert, K., K. Hessner, J. C. Nietro Borge, and J. Dittmer, WAMOS II: A radar based wave and current monitoring system, paper presented at *ISOPE '99*, Int. Soc. of Offshore and Polar Eng., Brest, France, May 1999.

Seiwell, H. R., Military oceanography in World War II, *Military Eng.*, *39*(259), 202–210, 1947.

Smith, R. A., and G. R. West, Airborne lidar: A surveying tool for the new millennium, in *Proceedings of Oceans '99* [CD-ROM], IEEE Press, Piscataway, N.J., 1999.

Stilwell, D., Jr., Directional energy spectra of the sea from photographs, *J. Geophys. Res.*, *74*, 1974–1986, 1969.

Stilwell, D., and R. O. Pilon, Directional spectra of surface waves from photographs, *J. Geophys. Res.*, *79*, 1277–1284, 1974.

Stockdon, H. F., and R. A. Holman, Estimation of wave phase speed and nearshore bathymetry from video imagery, *J. Geophys. Res.*, *105*, 22,015–22,034, 2000.

Teague, C. C., Multifrequency HF radar observations of currents and current shear, *IEEE J. Oceanic Eng.*, *OE-11*, 258–269, 1986.

Walker, R., *Marine Light Field Statistics*, pp. 6, 404, John Wiley, New York, 1994.

Williams, J. Z., and J. P. Dugan, Bathymetry measurements using electro-optical remote sensing, paper presented at *4th International*

Conference on Remote Sensing for Marine and Coastal Environments, Environ. Res. Inst. of Mich., Orlando, Fla., March 17–19, 1997.
Williams, W. W., The determination of gradients on enemy-held beaches, *Geogr. J.*, *XIC*, 76–93, 1946.
Wu, J., and J. T. Juang, Application of satellite images to the determination of coastal topography, in *Proceedings of 25th International Coastal Engineering Conference*, edited by B. Edge, pp. 3762–3769, Am. Soc. of Civ. Eng., 1996.
Young, I. R., W. Rosenthal, and F. Ziemer, A three-dimensional analysis of marine radar images for the determination of ocean wave directionality and surface currents, *J. Geophys. Res.*, *90*, 1049–1059, 1985.

J. P. Dugan, C. C. Piotrowski, and J. Z. Williams, Areté Associates, 1725 Jefferson Davis Highway, Suite 703, Crystal Square 2, Arlington, VA 22202. (dugan@arete-dc.com).

(Received April 14, 2000; revised March 9, 2001;
accepted March 19, 2001.)